

# Highly Selective Voltammetric Sensor for L-Tryptophan Using Composite-Modified Electrode Composed of CuSn(OH)<sub>6</sub> Microsphere Decorated on Reduced Graphene Oxide

Arumugam Sangili,<sup>1</sup> Venkatachalam Vinothkumar,<sup>1</sup> Shen-Ming Chen,\* Pitchaimani Veerakumar,\* Chia-Wei Chang, I. Panneer Muthuselvam, and King-Chuen Lin\*



Cite This: <https://dx.doi.org/10.1021/acs.jpcc.0c07197>



Read Online

ACCESS |

Metrics & More

Article Recommendations

Supporting Information

**ABSTRACT:** In this study, a nanostructured CuSn(OH)<sub>6</sub> microsphere decorated on reduced graphene oxide (CSOH/rGO) was prepared by a co-precipitation method followed by ultrasonication, which was used for the sensitive and selective determination of L-Tryptophan (L-Trp) in the presence of uric acid. Its structure and morphology were characterized by X-ray diffraction (XRD), field emission scanning/transmission electron microscopy (FE-SEM/TEM), Fourier transform infrared (FT-IR) spectroscopy, Brunauer–Emmett–Teller (BET) analysis, and X-ray photoelectron spectroscopy (XPS). Galvanostatic charge/discharge tests, cyclic voltammetry (CV), electrochemical impedance spectroscopy (EIS), and differential pulse voltammetry (DPV) methods have also been employed to investigate the electrochemical performance of the CSOH/rGO composite. Analytical parameters such as loading amount of catalyst, scan rate, pH value, cyclic stability, repeatability, and reproducibility were optimized. The CSOH/rGO composite shows excellent detection of L-Trp in a wide dynamic linear range (WLR) of 0.05–175.8 μM, a low limit of detection (LOD) of 2.0 nM, a limit of quantification (LOQ) of 68.9 nM, and a sensitivity of 0.21 μA μM<sup>-1</sup> cm<sup>-2</sup>. The fabricated electrode was further used to monitor the selectivity of L-Trp in the presence of uric acid and applied to the detection of L-Trp in spiked real samples with satisfactory results.



## INTRODUCTION

In recent years, metal hexahydroxystannate (MSn(OH)<sub>6</sub>; MHS; M = Zn, Co, Sr, Ca, and Cu) with d<sup>10</sup>–d<sup>10</sup> configuration, belonging to the perovskite family, has been found to have excellent physical and chemical properties due to its special cell structure.<sup>1,2</sup> It is a kind of transition-metal stannite possessing various morphologies sizes and shapes. As is well known, it can be used in a number of areas, such as gas, optical, and magnetic sensors,<sup>3–5</sup> photocatalysts,<sup>6</sup> and so on, owing to its intrinsic merits, including large specific surface area, cost-effectiveness, environmental friendliness, morphological diversity, and high catalytic activity. It is expected that the MHS materials would significantly improve the electrocatalytic properties, stability, and reproducibility of the electrode, as well as further reduce drawbacks in overpotential but increase the reaction rate.<sup>7</sup> In addition, MHS provides more adsorption and active sites, thus benefiting the affinity toward the analytes and exhibiting good catalytic activity. Copper hexahydroxystannate (CuSn(OH)<sub>6</sub>), with a structure of ReO<sub>3</sub> derivative,<sup>8–10</sup> has been widely applied in photocatalysis,<sup>11</sup> supercapacitors,<sup>12</sup> and batteries.<sup>13</sup> Compared to the different synthesized methods, the co-precipitation method is convenient and straightforward to synthesize CuSn(OH)<sub>6</sub> (CSOH will be used hereafter) microspheres/microcubes and nanocubes.<sup>14,15</sup> The superior electrocatalytic activity observed for CSOH is because the metal ions are

octahedrally coordinated with OH to form Cu(OH)<sub>6</sub> and Sn(OH)<sub>6</sub> polyhedra that connect with each other by sharing O atoms to build the whole crystalline structure.<sup>16</sup> Because they have different Shannon radii, this type of hydroxides showing multiple crystalline symmetries are widely used as electrode catalysts for sustainable applications. Nevertheless, only few reports on the applications of perovskite-type hydroxide for the electrochemical detection of biomolecule are available. By preparing the perovskite using a simple co-precipitation method, Subbarayan and co-workers demonstrated that the perovskite-based CoSn(OH)<sub>6</sub> nanocube-modified screen-printed carbon electrode (SPCE) exhibited good activity as rutin sensors.<sup>17</sup> Moreover, the fabrication of CSOH by chemical co-precipitation is considered as the most facile process for the low-temperature synthesis of the perovskite with defined crystallinity.<sup>5,11,14,15</sup> Low-temperature synthesis in aqueous solution is highly desirable because it represents an environ-

Received: August 6, 2020

Revised: October 16, 2020

ment- and user-friendly approach, which may be considered to be a relatively green chemical alternative of practical significance.

Recently, graphene (Gr) and reduced graphene oxide (rGO) have been used to determine the sensitivities for various drug molecules owing to their excellent conductivity, which results from  $\pi-\pi$  stacking and synergetic effects with other materials.<sup>18</sup> When biomolecules are adsorbed on the graphene surface, charge is transferred to or from the molecules to bring about a change of its Fermi level, thereby making electron transfer easier.<sup>19</sup> More specifically, their advantages such as extraordinary electrochemical properties, high surface area, and high charge-carrier mobility have drawn the interest and attention worldwide. It was reported that rGO has been applied as an effective sensing platform for selective detection of bioentities.<sup>20</sup> The layered structure of rGO electrodes can restrict ion conduction pathways and lead to a delay in ion migration. Therefore, rGO should be mixed with other materials such as conducting polymers, metal/metal oxides, and other carbon nanostructures to improve its ionic and electronic conduction.<sup>21</sup> Furthermore, to further promote their electrocatalytic properties, CSOH materials normally integrated with carbons are effective, which could accelerate electron transfer, resulting in greatly improved electrocatalytic performances. To date, a variety of rGO-based composites containing metal oxide nanoparticles such as TiO<sub>2</sub>,<sup>22</sup> ZnWO<sub>4</sub>,<sup>23</sup> CuSnO<sub>3</sub>@Cu<sub>2</sub>O,<sup>24</sup> and CuCo<sub>2</sub>O<sub>4</sub><sup>25</sup> have been successfully applied to electrochemical sensors.

Amino acids are well known to play a significant role in human and animal neuroregulation, organ development, and metabolism.<sup>26,27</sup> L-Tryptophan (L-Trp) is one of the eight essential amino acids for human's normal daily activity, including brain functions and neuronal regulatory mechanisms.<sup>28</sup> Many reports find that serotonin and melatonin are related to L-Trp. When L-Trp is improperly metabolized, toxic metabolites are produced in the brain to probably cause schizophrenia, drowsiness, nausea, hallucinations, headache, loss of appetite, and Parkinson's disease.<sup>29</sup> Unfortunately, the amount of L-Trp in vegetables and fruits is inadequate. As humans and animals cannot synthesize L-Trp themselves, it must be obtained from food and pharmaceutical formulas. The World Health Organization (WHO) recommends an L-Trp intake of 4 mg kg<sup>-1</sup> per day. However, excessive L-Trp may produce toxic waste in the brain, causing delusions and hallucinations.<sup>30</sup> Therefore, detection of L-Trp for preventing brain diseases is more significant.

Several techniques have been reported for the determination of L-Trp, including high-performance liquid chromatography (HPLC),<sup>31</sup> spectrophotometry,<sup>32</sup> capillary electrophoresis,<sup>33</sup> fluorometric micromethod,<sup>34</sup> and flow-injection chemiluminescence.<sup>35</sup> In addition, L-Trp is an electroactive substance that can be detected by electrochemical methods.<sup>36,37</sup> Electroanalytical techniques have the advantages of simplicity, portability, selectivity, and sensitivity. They attract great attraction for L-Trp monitoring in various sample matrices. However, direct oxidation of L-Trp on the bare electrode is not practical because of slow electron transfer and high overpotential, as well as poor repeatability due to the fouling effect. Such an unmodified electrode is inadequate for highly sensitive detection of L-Trp due to its sluggish electron transfer and less active sites. Therefore, various research studies have been reported for electrochemical sensing of L-Trp with electrode modification. For instance, Mattioli et al.<sup>38</sup> fabricated gold nanoparticles (Au NPs) electrodeposited onto the surface of a graphite-

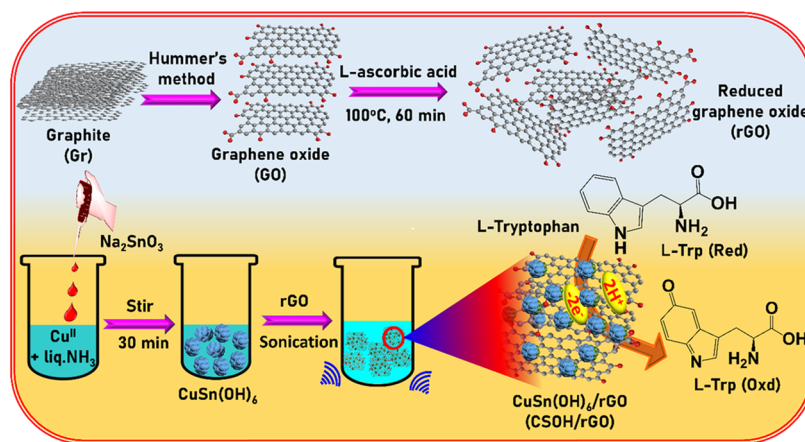
polyurethane composite (EGPU-tAuNP) electrode for the electrochemical determination of L-Trp. It exhibits a wide linear range (WLR) up to 0.6–2.0 ( $\mu\text{mol L}^{-1}$ ) and a limit of detection (LOD) of 0.053  $\mu\text{mol L}^{-1}$ . Likewise, Deng et al.<sup>39</sup> reported the acetylene black paste electrode with graphene (GR/ABPE) composite for the sensitive and selective determination of L-Trp, which delivered a WLR of 0.1  $\mu\text{M}$ –0.1 mM with an LOD of 60 nM for L-Trp. On the other hand, Tian et al. developed a molecularly imprinted chitosan film for an electrochemical sensor obtaining WLRs of 0.01–4, 4–20, and 20–100  $\mu\text{M}$  by second-derivative linear sweep voltammetry (LSV) and an LOD of 8.0 nM.<sup>40</sup> Xia et al. developed an electrochemical sensor based on Ag-MoS<sub>2</sub>/CS nanocomposites for the sensitive and selective determination of L-Trp. The linear range of the Ag-MoS<sub>2</sub>/CS sensor was 0.5–120  $\mu\text{M}$ , with an LOD of 0.05  $\mu\text{M}$  (S/N = 3).<sup>41</sup> However, to the best of our knowledge, the design and fabrication of electrochemical sensors for L-Trp detection using the CSOH/rGO composite have not been reported.

In this work, the CSOH/rGO composite was synthesized via a simple co-precipitation method followed by ultrasonication. The as-synthesized CSOH/rGO was further applied for sensitive and selective detection of L-Trp sensor for the first time. The unique properties of CSOH/rGO in the composites invoked a synergistic activity and thus effectively improved the electrochemical detection of L-Trp. The CSOH/rGO composite was characterized by electrochemical impedance spectroscopy (EIS), cyclic voltammetry (CV), and differential pulse voltammetry (DPV) techniques. Furthermore, the CSOH/rGO nanocomposite exhibits high catalytic activity, a large surface area to enhance the electron transfer between the modified electrode surface and the L-Trp, and excellent sensing performance for L-Trp detection. CSOH/rGO was fabricated as a modified electrode for the electrochemical detection of L-Trp, and the results were discussed in terms of WLR and LOD at the neutral pH and could be successfully applied to detect the L-Trp level in human urine samples.

## EXPERIMENTAL SECTION

**Materials and Electrolytes.** Sodium stannate trihydrate ( $\text{Na}_2\text{SnO}_3 \cdot 3\text{H}_2\text{O}$ , 95%), copper(II) sulfide pentahydrate ( $\text{CuSO}_4 \cdot 5\text{H}_2\text{O}$ , ACS reagent,  $\geq 98.0\%$ ), liquid ammonia (25 wt % liq. NH<sub>3</sub>) solution (25 wt %), L-Tryptophan (L-Trp,  $\text{C}_{11}\text{H}_{12}\text{N}_2\text{O}_2$ ,  $\geq 98\%$  (HPLC), solid), uric acid ( $\text{C}_5\text{H}_4\text{N}_4\text{O}_3$ ,  $\geq 99\%$ ), and potassium ferricyanide ( $\text{K}_3[\text{Fe}(\text{CN})_6]$ , 98%) were purchased from Sigma-Aldrich. All other chemicals (including interfering species) used in this experiment were of analytical grade. All required aqueous solutions were prepared using ultrapure water ( $\geq 18.2 \text{ M}\Omega \text{ cm}$ ) produced by a Millipore system. The supporting electrolyte, 0.05 M phosphate buffer (PB), was prepared through homogeneous mixing of sodium hydrogen phosphate ( $\text{Na}_2\text{HPO}_4$ ) and monosodium phosphate ( $\text{NaH}_2\text{PO}_4$ ) followed by optimization of the pH value using 0.1 M H<sub>2</sub>SO<sub>4</sub> and NaOH.

**Characterization.** The crystalline nature and phase purity of the as-synthesized CSOH microsphere were examined using the X-ray diffraction (XRD) patterns obtained from a PANalytical X'Pert Pro diffractometer (X'Pert PRO, Malvern, Worcestershire, U.K.) with Cu K $\alpha$  radiation ( $\lambda = 0.1541 \text{ nm}$ ) in the range of 10–80°. The morphology, microstructure, and mapping analyses of the material were made using field emission gun scanning electron microscopy (FE-SEM) (JEOL JSM-6500F, Akishima, Tokyo, Japan), whereas high-resolution transmission electron microscopy (HR-TEM) was conducted using a

**Scheme 1.** Schematic Illustration of the Synthesis and Electrochemical Process of CSOH/rGO for the Detection of L-Tryptophan

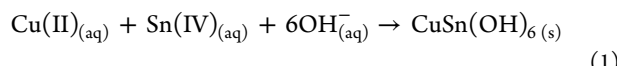
Shimadzu JEM-1200 EX at an accelerating voltage of 200 kV coupled with elemental mapping (energy-dispersive X-ray spectrometry–EDX) using a HORIBA EMAX X-ACT. Fourier transform infrared (FT-IR) spectra were recorded on a Jasco CHI1000C FT-IR-6600 spectrometer using the KBr pellet method in the range of 400–4000 cm<sup>-1</sup>. The surface areas were determined by adsorption data in the relative pressure ( $P/P_0$ ) range of 0.48–0.85 using the Brunauer–Emmett–Teller (BET) method accompanied by a Quantachrome Autosorb-1 volumetric adsorption analyzer at -196 °C (77 K). The structural and compositional information of the composite was obtained using X-ray photoelectron spectroscopy (XPS) in a Thermo ESCALAB 250 system.

Electrochemical characterization was executed in a three-electrode cell system containing a modified glassy carbon electrode (GCE; active surface area: 0.0729 cm<sup>-2</sup>) as the working electrode, a platinum (Pt) wire as the counter electrode, and Ag/AgCl as the reference electrode, based on an electrochemical workstation (CHI400 and CHI120Sb, Shanghai Chenhua, China). L-Trp sensing was performed by cyclic voltammetry (CV) and differential pulse voltammetry (DPV) methods. Electrochemical impedance spectroscopy (EIS) was examined by 5.0 mM [Fe(CN)<sub>6</sub>]<sup>3-/4-</sup> containing 0.1 M KCl in the range of 100 MHz to 100 kHz. IM6ex ZAHNER Elektrik (version, Thales 4.01, Z Simp Win EIS DATA analysis software) was used to analyze the detected EIS data.

**Preparation of CSOH/rGO Composite.** The GO and rGO were prepared from the oxidation of graphite by the modified Hummers' method (see the Supporting Information).<sup>42</sup> CSOH microspheres were synthesized as follows.<sup>43</sup> Typically, 50 mL of 0.12 M CuSO<sub>4</sub>·5H<sub>2</sub>O solution and Liq. NH<sub>3</sub> (25 wt %) were dropwise added under stirring condition until blue precipitation disappeared. Finally, a homogeneous dark blue solution was obtained. Then, 50 mL of 0.05 M Na<sub>2</sub>SnO<sub>3</sub>·3H<sub>2</sub>O solution was added dropwise into the above mixture, followed by stirring for 30 min at room temperature. Subsequently, a light blue precipitate was collected, and then washed with Millipore water and ethanol several times. Finally, the precipitate was dried at 60 °C for 12 h in an oven. For the preparation of the CSOH/rGO composite, CSOH particles were immobilized on the rGO support by direct ultrasonication. In brief, 10 mg of the as-prepared rGO sample was dispersed in ultrapure water (10 mL), followed by adding 50 mg of CSOH under ultrasonic vibration for at least 1 h, and the resultant CSOH incorporated with rGO composite was denoted as CSOH/rGO (see Scheme

1). Finally, the black product was dried in vacuum at 40 °C overnight.

The synthesis of CSOH microsphere structures is highly repeatable and could be prepared by co-precipitation in an aqueous solution. As given in eq 1, perovskite-type CSOH was first prepared in an aqueous solution by fast stoichiometric co-precipitation of Cu(II), Sn(IV), and OH<sup>-</sup>. The formation of CSOH microspheres resulted from its intrinsic tetragonal crystal structure.<sup>44</sup> For the overall process, the major chemical processes involved might be described as follows



**Fabrication of CSOH/rGO/GCE.** First, the glassy carbon electrode (GCE) was polished using 0.05 μm alumina slurry, repeatedly washed with Millipore water and ethanol, and dried before use. Next, the suspension of the CSOH/rGO composite was prepared by adding 5.0 mg of CSOH/rGO materials to 1.0 mL of Millipore water for 15 min sonication. Subsequently, 6.0 μL of the dispersion was drop-cast onto the surface of pretreated GCE and dried at 50 °C to complete the fabrication of electrode. Finally, the obtained CSOH/rGO/GCE was performed in electrochemical experiments.

## RESULTS AND DISCUSSION

**Characterization of CSOH Microsphere.** The X-ray diffraction (XRD) patterns of the CSOH microsphere materials are shown in Figure 1a. The XRD pattern at 2θ of about 19.8, 21.9, 23.4, 32.2, 37.5, 40.3, 44.6, 48.0, 51.2, 53.4, 54.1, 59.1, and 67.8° can be indexed as the (111), (022), (200), (202), (311), (222), (321), (400), (204), (402), (420), (422), and (404) planes for CSOH microsphere (JCPDS 20-0369).<sup>43,44</sup> These

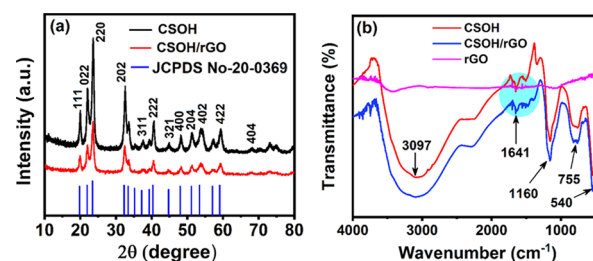


**Figure 1.** XRD patterns of CSOH and CSOH/rGO composite and (b) FT-IR spectra of rGO, CSOH, and CSOH/rGO composite.

results indicate that CSOH has been successfully formed. In the XRD pattern of CSOH/rGO, no diffraction peak is assigned to rGO, because the loading of low mass has lower crystallinity or amorphous nature. However, the rGO is further confirmed by FE-SEM and TEM-EDX with elemental mapping analysis (*vide infra*). This result indicates that the surface of the CSOH microsphere is decorated with rGO sheets. From the full width at half-maximum of the peak (111), the volume-averaged particle size was estimated by Scherrer's eq 2

$$D = \frac{0.89\lambda_{K\alpha}}{B_{2\theta} \cos \theta_{\max}} \quad (2)$$

where  $D$  is the mean size of the CSOH microsphere,  $\lambda_{K\alpha}$ ,  $\theta_{\max}$ , and  $B_{2\theta}$ , respectively, represent the X-ray wavelength (Cu  $K\alpha$   $\lambda_{K\alpha} = 1.54056 \text{ \AA}$ ), the maximum angle of the XRD peak, and the half-peak width for CSOH (111) in radians. The CSOH particle size is 34.5 nm.

**Figure 1b** presents the FT-IR spectra of rGO, CSOH, and CSOH/rGO. The peak at  $540 \text{ cm}^{-1}$  belongs to the stretching vibration of Sn—O. The sharp peak observed at  $755 \text{ cm}^{-1}$  is due to water–water hydrogen bonding, and  $1160 \text{ cm}^{-1}$  is attributed to the Sn—OH bending vibration. The peaks at  $1641$  and  $3097 \text{ cm}^{-1}$  are attributed to the —OH bending and the stretching vibration, respectively. These results appear similar to the previous report,<sup>5</sup> further confirming that the as-synthesized material is CSOH. There is no intense peak observed for rGO. For the CSOH/rGO composite, the peak intensity around  $1200$ – $1600 \text{ cm}^{-1}$  became decreased and slightly shifted,<sup>45</sup> demonstrating the interaction between CSOH and rGO sheets.

FE-SEM and TEM analyses determined the size and morphology of the as-prepared CSOH and CSOH/rGO composites. **Figure 2a–c** displays CSOH nanoparticles that

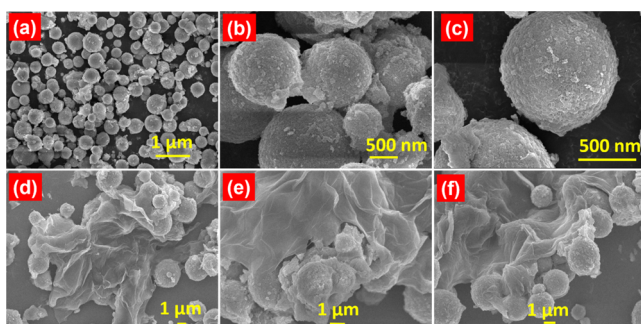


**Figure 2.** (a–c) Typical FE-SEM images of the CSOH microsphere and (d–f) CSOH/rGO composite.

shows the unevenly formed nanoparticles and agglomerations. The CSOH microspheres are displayed with different magnification, showing that the sphere-like structure was successfully synthesized. The EDX mapping analysis of CSOH showed that elements of Cu, Sn, and O were homogeneously distributed throughout the microsphere (**Figure S1**). As shown in **Figure 2d–f**, the FE-SEM image of the CSOH/rGO composite identifies the spherical shape of CSOH grew on the surface of rGO sheets.

The typical FE-TEM images of the CSOH microsphere with different magnifications are shown in **Figure S2**. From the FE-TEM images, it was found that the CSOH materials have spherical morphology showing the qualitative and quantitative elemental composition. The percent elemental composition of the CSOH microsphere, obtained from the EDX analysis, is also

shown in **Figure S2**. It was found that the CSOH microsphere had about 27.19% oxygen, 37.69% metallic copper, 33.17% metallic tin, and a trace amount (1.95%) of carbon. **Figure 3** shows the different magnifications of the FE-TEM image and mapping analysis of the rGO/CSOH composite. The results show that the surface of CSOH is entirely shielded with wrinkle rGO (**Figure 3a–f**). Additionally, CSOH was decorated on the surface of rGO, forming a core–shell-like structure. This structure could help disperse the rGO homogeneously in CSOH composite and enhance its interfacial compatibility. Furthermore, the elemental composition of the as-prepared CSOH/rGO composite was also confirmed by EDX analysis (**Figure S3**). The resulting peak intensities and percentages of Cu, Sn, O, and C are 37.20, 33.22, 19.57, and 9.50%, respectively. The EDX mapping analysis showed that four elements of Cu, Sn, O, and C (**Figure 3g–j**) were homogeneously distributed throughout the microsphere.

**X-ray Photoelectron Spectroscopy.** In addition, X-ray photoelectron spectroscopy (XPS) is used to further analyze the elemental composition and valence states of the CSOH/rGO composite. As depicted in **Figure 4a**, the XPS survey spectrum of CSOH/rGO indicates the occurrence of C, O, Cu, and Sn elements. **Figure 4b** displays the high-resolution Cu 2p spectrum systematically deconvoluted into four peaks with binding energies (BE) of 936.6 eV (Cu 2p<sub>3/2</sub>) and 956.4 eV (Cu 2p<sub>1/2</sub>), as well as their concomitant shake-up lines at 944.0 and 964.0 eV, respectively. The above XPS result can convincingly confirm the +2 oxidation state of copper existing in Cu(OH)<sub>2</sub> rather than CuO on the surface of Sn(OH)<sub>6</sub>, according to the previous report.<sup>43</sup> Thereof, it is indicated that the chemical state of Cu(II) was ascribed to the 3d<sup>9</sup> configuration in its ground state. The XPS spectra of Sn 3d (**Figure 4c**) showed two main peaks at 486.80 and 495.23 eV, arising from Sn<sup>4+</sup>, which corresponds to CuSn(OH)<sub>6</sub>. The C 1s spectrum (**Figure 4d**) can be fitted to four peaks at BE of 284.7 eV (C=C), 285.3 eV (C–C), 286.2 eV (C–O/C=O), and 288.6 eV (O–C=O), which are directly associated with rGO. As can be seen in **Figure 4e**, the O 1s spectrum can be fitted into two peaks detected at BEs of 533.6 and 532.1 eV for the CuSn(OH)<sub>6</sub>/rGO sample, which can be attributed to C–OH and C=O/O=C–OH coordinations, respectively.

**BET Surface Area.** Generally, porous materials with higher specific surface areas and large pore volumes are beneficial for the enhancement of electrochemical sensing performance due to the presence of more surface active sites for the adsorption of reactant molecules, ease of transportation of reactant molecules and products through the interconnected porous networks, and rapid electron transfer. Therefore, the BET surface area of the as-prepared CSOH/rGO composite was investigated by the nitrogen adsorption–desorption measurement, as displayed in **Figure S4**. The specific surface area of the CSOH/rGO composite is  $18.775 \text{ m}^2 \text{ g}^{-1}$ , and the pore volume is  $0.0523 \text{ cm}^3 \text{ g}^{-1}$ , which may not greatly affect the electrochemical performance because this level of porosity is enough for the free diffusion of guest molecules throughout the electrocatalysts.

**Electrochemical Characterization of CSOH/rGO.** Electrochemical characteristics, such as electrochemical interfacial and electron ( $e^-$ ) transfer properties, were investigated. EIS is a powerful method for measuring electrochemical surface properties at the electrolyte interface of the synthesized material. **Figure 5a** displays the EIS spectra of the proposed electrode in 0.1 M KCl/5.0 mM [Fe(CN)<sub>6</sub>]<sup>3−/4−</sup> and Randel's equivalent circuit model (**Figure 5a**, inset), where  $Z_w$  is the Warburg impedance,

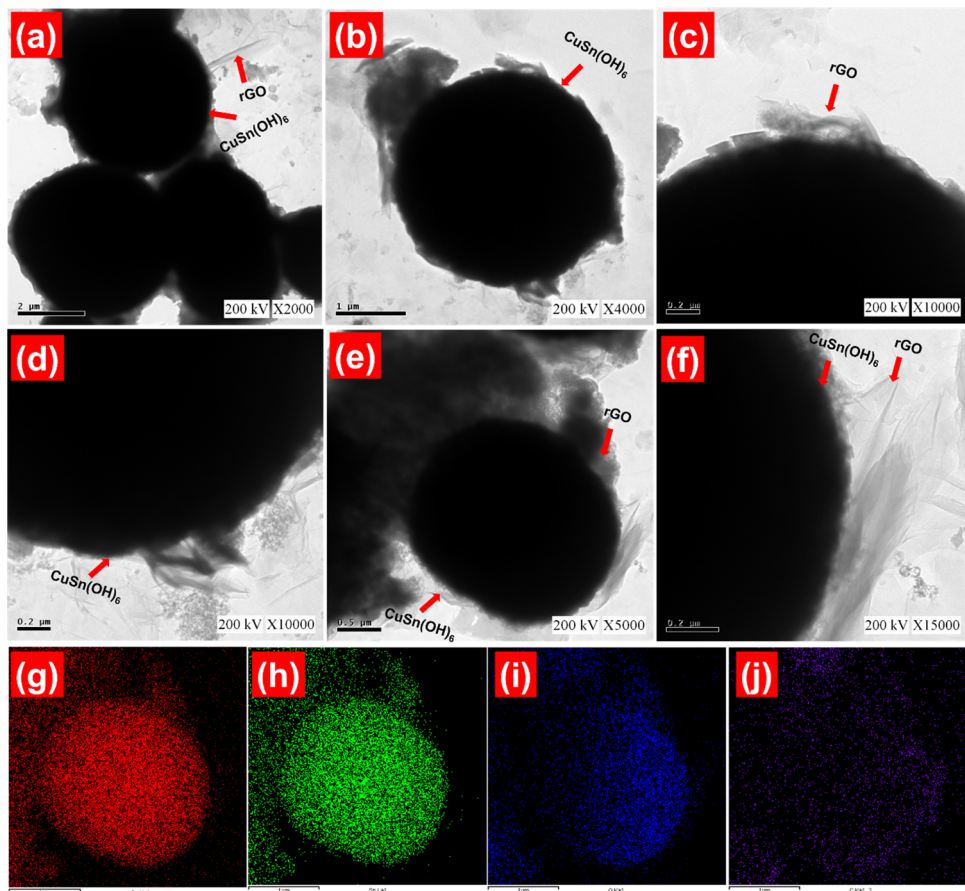


**Figure 3.** (a–f) TEM images of CSOH/rGO composite with different magnifications and EDX mapping elements of (g) Cu, (h) Sn, (i) O, and, (j) C.

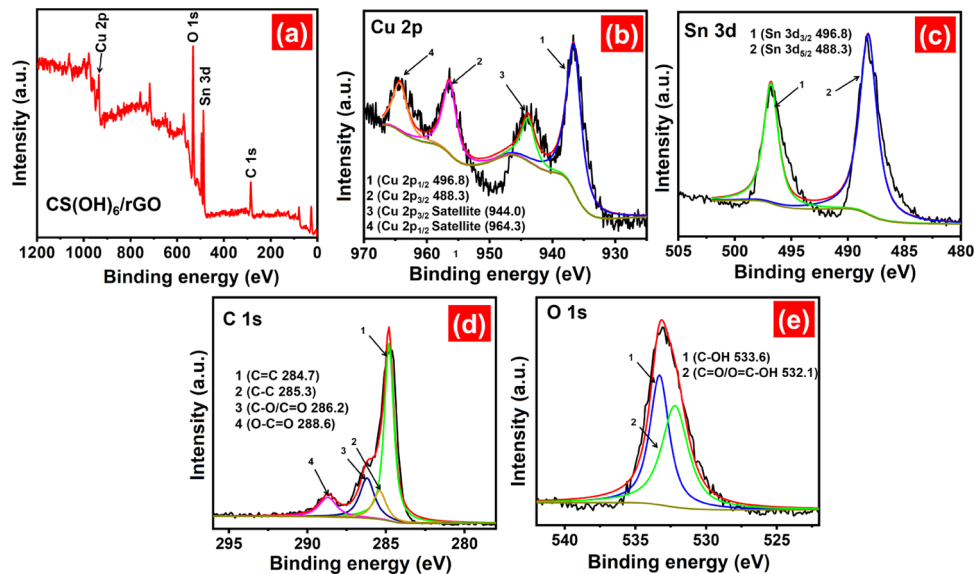


**Figure 4.** (a) XPS survey spectrum CSOH/rGO composite and XPS spectra of (b) Cu 2p, (c) Sn 3d, (d) C 1s, and (e) O 1s.

$R_{ct}$  is the interfacial electron transfer resistance,  $R_s$  is the electrolyte solution resistance, and  $C_{dl}$  is the double-layer resistance. The  $R_{ct}$  value was calculated from the diameter of a semicircle, and the straight line of the plots reflects the value of  $R_s$ . The bare GCE, rGO,  $\text{Sn}(\text{OH})_2$ , CSOH, and CSOH/rGO gave rise to  $R_{ct}$  values of 729, 1254, 1492, 1174, and  $434\ \Omega$ , respectively. The EIS results show that the obtained semicircle for GCE appeared at higher frequencies with a small interface

impedance. A large impedance value observed for rGO/GCE and  $\text{Sn}(\text{OH})_2/\text{GCE}$  could be attributed to the presence of negatively charged functional groups on the rGO nanosheets to block the diffusion of  $\text{K}_3\text{Fe}(\text{CN})_6/\text{K}_4\text{Fe}(\text{CN})_6$  (1:1) from solution to electrode surface. In addition, when CSOH is used to construct a semiconductor electrode (Figure 5a, curve (iv)), this material suffers from the electrostatic repulsion between negative charges of the CSOH and the electroactive probe

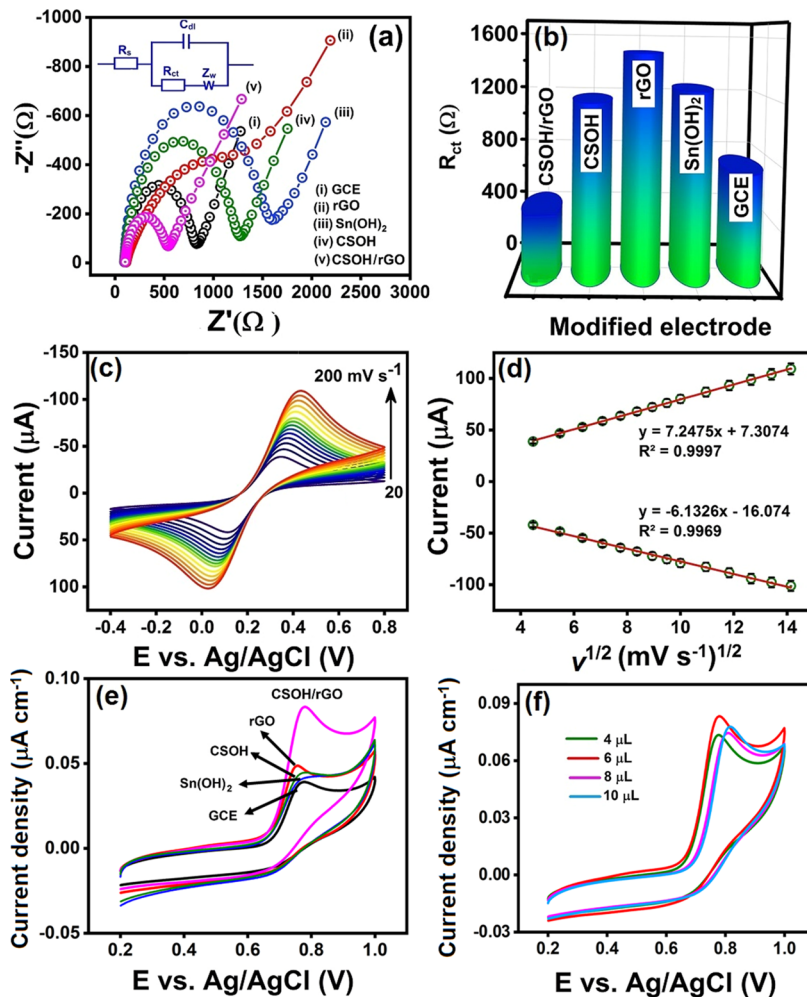


**Figure 5.** (a) EIS spectra (inset: Randles circuit model), (b) the corresponding bar diagram of bare GCE,  $\text{Sn}(\text{OH})_2/\text{GCE}$ , CSOH/GCE, rGO/GCE, and CSOH/rGO/GCE in 0.1 M KCl/5mM  $[\text{Fe}(\text{CN})_6]^{3-/4-}$ , (c) different scan rates (20–200  $\text{mV s}^{-1}$ ) of CSOH/rGO/GCE, (d) linear plot of redox peak current versus square root of scan rate, (e) CVs of the bare GCE,  $\text{Sn}(\text{OH})_2$ , rGO, CSOH, and CSOH/rGO/GCE in the presence of  $75 \mu\text{M L-Trp}$ , and (f) loading amount of CSOH/rGO-modified electrode in  $75 \mu\text{M L-Trp}$  in  $\text{N}_2$ -purged 0.05 PB (pH 7.0) at  $50 \text{ mV s}^{-1}$ .

$[\text{Fe}(\text{CN})_6]^{3-/4-}$ .<sup>46,47</sup> On introducing copper into  $\text{Sn}(\text{OH})_2$ , the semicircle diameter range decreased. The CSOH/rGO/GCE is found to have relatively faster electron transfer properties and better electrocatalytic activity than other electrodes.<sup>48</sup> We take a further step to compare the prepared composite with commercial (C) carbon derivatives (see Figure S5). The obtained  $R_{\text{ct}}$  values of the modified electrodes such as C-GO, C-graphite (C-GT), C-rGO, C-graphene (C-GR), and prepared CSOH are 657, 706, 650, and  $322 \Omega$ , respectively. The C-GR/CSOH-modified electrode was found to have a smaller  $R_{\text{ct}}$  value compared with the as-prepared composites. Graphene is more conductive than rGO. In this work, we have selected rGO/CSOH-modified electrode for the determination of L-Trp. One reason is that rGO is a better working electrode modifier for constructing electrochemical sensors than both GO and GR, because it contains both the GO negatively charged groups and the excellent conductive properties of GR. The functional groups on the rGO surface act as effective anchoring sites to immobilize various active species compared with graphene. This result explains that the as-prepared CSOH/rGO/GCE has relatively faster electron transfer properties and better electrocatalytic activity than commercial carbon derives.

The CV characterizes the electroactive surface area of the CSOH/rGO electrode (Figure 5c) at different scan rates from

20 to 200  $\text{mV s}^{-1}$ . Obviously, the square root of the scan rate increases with increasing oxidation peak current (Figure 5d). The linear relationship follows:  $I_{\text{pa}} (\mu\text{A}) = 7.2475 (\nu^{1/2}) + 7.3074$  ( $R^2 = 0.9997$ ). Accordingly, the Randles–Sevcik equation is used to calculate the electroactive surface area, as expressed in eq 3<sup>49</sup>

$$I_{\text{pa}} = 2.69 \times 10^5 A \times D^{1/2} n^{3/2} C \nu^{1/2} \quad (3)$$

where  $I_{\text{pa}}$ ,  $D$ ,  $n$ ,  $A$ ,  $\nu$ , and  $C$  represent the oxidation peak current ( $\text{A}$ ), diffusion coefficient of 0.1 M KCl/5.0 mM  $[\text{Fe}(\text{CN})_6]^{3-/4-}$  ( $7.60 \times 10^{-6} \text{ cm}^2 \text{ s}^{-1}$ ), number of electron transfer ( $n = 1$ ), active surface area ( $\text{A}$ ), scan rate, and concentration ( $\text{mol cm}^{-3}$ ), respectively. As a consequence, the electroactive surface areas of bare GCE and CSOH/rGO/GCE electrodes are evaluated to be 0.0729, and  $0.35 \text{ cm}^2$ , respectively. Based on the electrochemical characteristics, the obtained results (such as reduced charge transfer resistance  $R_{\text{ct}}$  and high peak current as well as electroactive surface area) indicate that the fabricated CSOH/rGO electrode is superior for the detection of L-Trp. Therefore, given the obtained  $R_{\text{ct}}$  value, the charge transfer rate ( $k_s$ ) of bare GCE and CSOH/rGO-modified GCE was determined using eq 4<sup>50</sup>

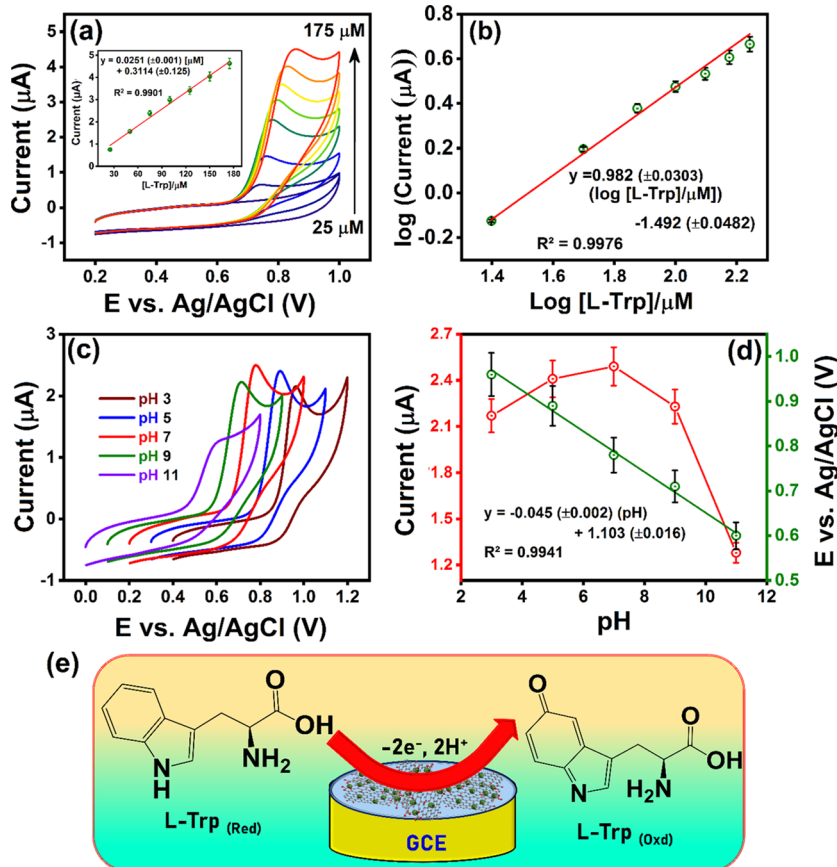


**Figure 6.** (a) CV curve of different concentrations of L-Trp (inset: plot of different concentrations versus peak current), (b) plot of log current versus log concentration, (c) CV response of CSOH/rGO/GCE in L-Trp (75  $\mu\text{M}$ ) in PB at different pHs (3.0, 5.0, 7.0, 9.0, and 11.0) at 50  $\text{mV s}^{-1}$ , (d) plot of the oxidation peak current (red line) and peak potential (green line) and pH, and (e) plausible mechanism of electro-oxidation of L-Trp at CSOH/rGO/GCE.

$$R_{ct} = \frac{RT}{n^2 F^2 k_s C} \quad (4)$$

where  $R$ ,  $T$ ,  $F$ ,  $A$ ,  $n$ ,  $C$ , and  $k_s$  represent the universal gas constant (8.314 J mol<sup>-1</sup> K<sup>-1</sup>), temperature (25 °C), Faraday constant (96 485 C mol<sup>-1</sup>), active surface area, number of electron transfer, concentration, and charge transfer rate, respectively. The  $k_s$  value was calculated to be  $4.51 \times 10^{-8}$  and  $1.21 \times 10^{-7}$  cm<sup>-1</sup> s<sup>-1</sup> for bare GCE and CSOH/rGO electrode, respectively.

**Electrochemical Performance of CSOH/rGO/GCE.** The electrochemical performance of L-Trp was investigated by CV on bare GCE, Sn(OH)<sub>2</sub>, CSOH, rGO, and CSOH/rGO-modified GCE containing PB (0.05 M, pH 7.0) at 50 mV s<sup>-1</sup> in the presence of L-Trp, as presented in Figure 5e. While with 75  $\mu\text{M}$  L-Trp in 0.05 M PB, CSOH/rGO/GCE displayed the highest peak current (2.52  $\mu\text{A}$ ) compared with bare GCE (1.17  $\mu\text{A}$ ), Sn(OH)<sub>2</sub>/GCE (1.45  $\mu\text{A}$ ), rGO/GCE (1.74  $\mu\text{A}$ ), and CSOH/GCE (1.56  $\mu\text{A}$ ). The modified electrode displayed oxidation peak potential at +0.76 V. The anodic peak has been known to undergo a two-proton and two-electron process for the irreversible oxidation of L-Trp.<sup>51–53</sup> Obviously, from the achieved results (Figure 5e), CSOH/rGO-modified GCE yields more significant electrocatalytic response than those by bare GCE, Sn(OH)<sub>2</sub>/GCE, rGO/GCE, and CSOH/GCE.

The effect of loading capacitance of CSOH/rGO dispersion drop-cast on the GCE was examined by different dosages (4.0, 6.0, 8.0, and 10.0 mg mL<sup>-1</sup> in DI water), as shown in Figure 5f. The result exhibited that the oxidation peak current response

(75  $\mu\text{M}$ , L-Trp) reached the maximum at 6.0 mg mL<sup>-1</sup> and then decreased on increasing the amount from 8.0 to 10.0 mg mL<sup>-1</sup>. These results indicated that the current response at 6.0 mg mL<sup>-1</sup> provides the highest performance-sensing condition for L-Trp.

**Electrochemical Activity CSOH/rGO/GCE. Effect of Concentration.** The determination of L-Trp at CSOH/rGO/GCE was investigated by changing the concentration of L-Trp from 0 to 175  $\mu\text{M}$  in N<sub>2</sub> saturated 0.05 M PB (pH 7.0) at 50 mV s<sup>-1</sup>. In Figure 6a, the CV response shows that the oxidation peak current increases with L-Trp. The linear regression equation between the oxidation peak current and different concentrations can be expressed as  $I_{pa}$  ( $\mu\text{A}$ ) = 0.025 C (L-Trp/ $\mu\text{M}$ ) + 0.3114 and  $R^2$  = 0.9901, as displayed in Figure 6a (inset), implying the behavior of the electrochemical activity of CSOH/rGO/GCE toward the L-Trp determination. Furthermore, the logarithmic plot of the oxidation peak current versus current is shown in Figure 6b. The corresponding regression equation is  $\log I_{pa}$  ( $\mu\text{A}$ ) = 0.982 ( $\pm 0.0303$ ) ( $\log [\text{L-Trp}/\mu\text{M}]$ ) - 1.492 ( $\pm 0.0482$ ), and correlation coefficient is  $R^2$  = 0.9976. The obtained slope value is approximately 1, indicating that the CSOH/rGO electrode follows the first-order kinetic process during the determination of L-Trp.

**Effect of pH.** The electrochemical determination of L-Trp and the response of faradic processes were critically influenced by pH. We monitor the effect of electrolyte solutions of different pHs on the electrochemical performance of L-Trp at the CSOH/rGO/GCE with 125  $\mu\text{M}$  L-Trp in 0.05 M PB. This buffer is an effective supporting electrolyte in the pH range of 3.0–11.0

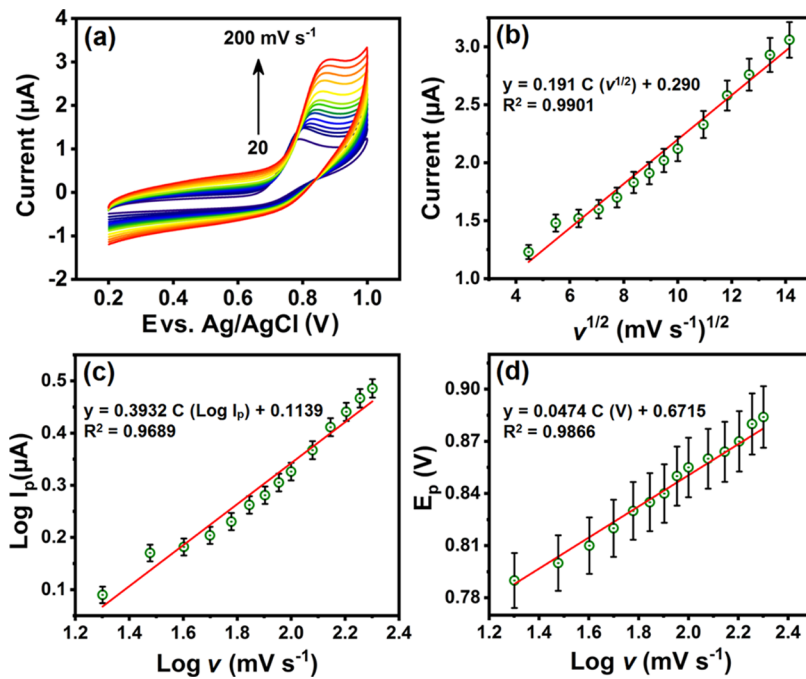


**Figure 7.** (a) CV response of  $50 \mu\text{M}$  L-Trp on CSOH/rGO/GCE at different scan rates ( $20, 30, 40, 50, 60, 70, 80, 90, 100, 120, 140, 160, 180$ , and  $200 \text{ mV s}^{-1}$ ) in PB ( $0.05 \text{ M}$ , pH 7.0). (b) Relationship between oxidation peak current versus square root of scan rate. (c) Plot between  $\log v$  ( $\text{mV s}^{-1}$ ) versus  $\log I_{\text{pa}}$  ( $\mu\text{A}$ ). (d) Calibration plot against  $\log v$  versus oxidation peak potential.

(Figure 6c). The oxidation peak potential ( $E_{\text{pa}}$ ) and the peak current ( $I_{\text{pa}}$ ) of L-Trp were obtained at the CSOH/rGO/GCE with various pH solutions containing  $75 \mu\text{M}$  L-Trp at a scan rate of  $50 \text{ mV s}^{-1}$ . The oxidation peak current of L-Trp increased from pH 3.0 to 11.0, and the maximum anodic peak current was at pH 7.0. Subsequently, pH 7.0 was considered as the optimal electrolyte solution for the determination of L-Trp, as illustrated in Figure 6c (red line). The anodic peak potential of L-Trp was also examined for the different pH solutions from 3.0 to 9.0. A linear plot was obtained following  $E_{\text{pa}}(\text{V}) = -0.045 \text{ C} (\pm 0.002)$  ( $\text{pH} + 1.103 (\pm 0.016)$  and  $R^2 = 0.9941$  (Figure 6d green line), indicating that the electrochemical activity of L-Trp at the CSOH/rGO/GCE was pH-dependent. The slope was determined as  $E_{\text{pa}}(\text{V}) - 45 \text{ mV pH}^{-1}$ , which was close to the theoretical value ( $-59 \text{ mV pH}^{-1}$  at  $25^\circ\text{C}$ ). The slope indicates that the proton-electron transfer mechanism is involved, according to eq 5<sup>54</sup>

$$\frac{dE_{\text{pa}}}{dE_{\text{pH}}} = \frac{2.303m}{n} \frac{RT}{F} \quad (5)$$

where  $m$  and  $n$  represent the number of protons and electrons, respectively, and  $R$ ,  $T$ , and  $F$  constants. The ratio  $m/n$  was calculated to be 0.75 for the detection of L-Trp. The obtained results are found to be almost equal to that suggested the equal number of electron and proton transfer in reactions. The plausible electrochemical oxidation mechanism of L-Trp at CSOH/rGO/GCE is shown in Figure 6e.<sup>55</sup>

**Effect of Scan Rate.** The influence of scan rate on the electrochemical oxidation of L-Trp ( $75 \mu\text{M}$ ) on CSOH/rGO/GCE at different scan rates ( $20 \rightarrow 200 \text{ mV s}^{-1}$ ) in  $0.05 \text{ M}$  PB (pH 7.0) is shown in Figure 7a. The irreversible anodic peaks were observed. The peak shifted toward more positive potential with an increase in scan rates. The potential shift is attributed to the formation of a complex compound for the L-Trp on the surface of CSOH/rGO. The linear plot of the square root of scan

rate versus oxidation peak current is shown in Figure 7b, yielding the equation  $I_{\text{pa}} = 0.191 \text{ C} + 0.2904$  ( $R^2 = 0.9901$ ). The results displayed that the electrochemical oxidation process of L-Trp on the surface of CSOH/rGO/GCE is diffusion-controlled. A logarithmic linear plot of scan rate versus anodic peak current gave a slope of 0.039 (Figure 7c), which is near the theoretical value of 0.5 (>10 times) for the purely diffusion-controlled process.<sup>56</sup> The electroactive species of L-Trp on CSOH/rGO diffuse from the bulk solution to the planar surface. The equation can be expressed as  $I_{\text{pa}} (\mu\text{A}) = 0.3932 (\pm 0.0203) \log v (\text{mV s}^{-1}) - 0.1139 (\pm 0.0386)$  ( $R^2 = 0.9689$ ). As the scan rate increases, the anodic peak potential shifted toward positive sides, indicating that the oxidation reaction of L-Trp tends to be irreversible on the modified electrode. The linear relationship of the anodic peak potential and logarithm of the scan rate can be depicted in Figure 7d, and the equation is expressed as  $E_{\text{pa}}(\text{V}) = 0.0294 \text{ C} - 0.6715$  ( $R^2 = 0.9866$ ). As for an irreversible electrode process, according to the Laviron method,  $E_{\text{pa}}$  is defined by eq 6<sup>57</sup>

$$E_{\text{pa}} = E^{0'} + \left( \frac{2.303RT}{anF} \right) \log \left( \frac{RTk^0}{anF} \right) + \left( \frac{2.303RT}{anF} \right) \log v \quad (6)$$

where  $E^{0'}$ ,  $k^0$ ,  $\alpha$ , and  $n$  represent the formal potential, heterogeneous rate constant, electron transfer coefficient, and number of electrons transferred, respectively. The linear plot of  $E_{\text{pa}}$  versus  $\log v$  achieved a slope of  $2.303RT/anF$ . Given the slope of 0.0894, the value of  $an$  is calculated to be 1.25. According to eq 7,<sup>58</sup> the calculated  $\alpha$  is 0.72.

$$\alpha = \frac{47.7}{E_p - E_{p/2}} \text{ mV} \quad (7)$$

where  $E_p$  and  $E_{p/2}$  represent the formal potential and half of the formal potential value. Further, the number of electrons transferred in the oxidation of L-Trp was calculated to be 2.

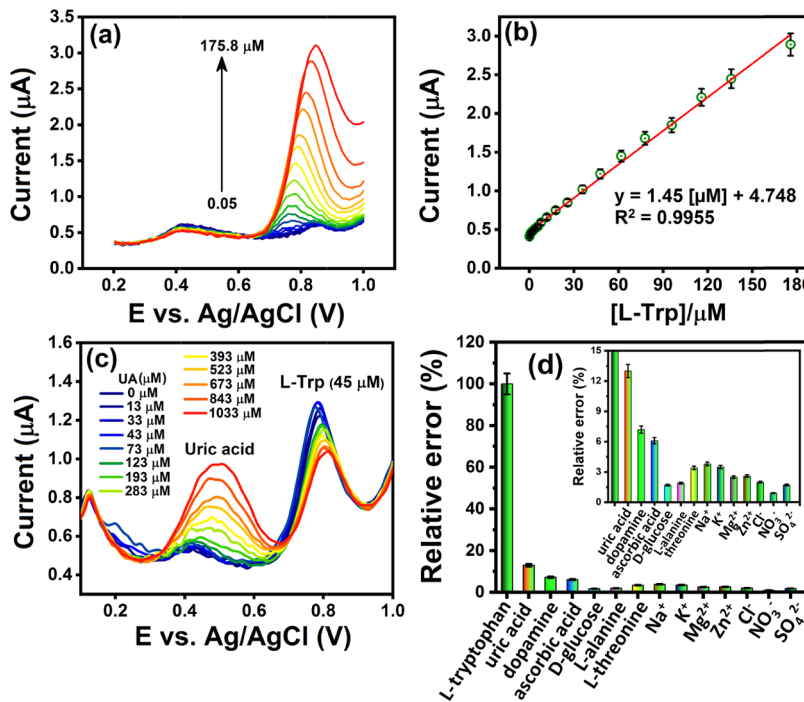


**Figure 8.** (a) DPV profiles of CSOH/rGO/GCE at different L-Trp concentrations in the 0.05 M PB (pH 7.0) (0.05, 0.2, 0.6, 1.3, 2.3, 3.8, 5.8, 7.8, 11.8, 17.8, 25.8, 35.8, 47.8, 61.8, 77.8, 95.8, 115.8, 135.8, and 175.8  $\mu\text{M}$ ). (b) Calibration curve between different concentrations of L-Trp and oxidation current. (c) Simultaneous detection of uric acid (concentration range: 0–1033  $\mu\text{M}$ ) and L-Trp. (d) Selectivity of the fabricated sensor (inset: a preview of interference).

**Table 1. Comparison of L-Trp Determination over Various Modified Electrodes**

electrode	WLR ( $\mu\text{M}$ )	LOD ( $\mu\text{M}$ )	sensitivity ( $\mu\text{A } \mu\text{M}^{-1}$ )	ref
TBAB... <sup>a</sup> $\beta$ -CD/MWCNTs/GCE	1.5–30.5	0.07		<sup>28</sup>
Ag@C <sup>b</sup> /GCE	0.1–100	0.04		<sup>54</sup>
Cys-AuNp-GW <sup>c</sup>	0.85–1200	0.0185	0.1198	<sup>55</sup>
Au NPs <sup>d</sup> /GCE	0.9–50	0.08		<sup>58</sup>
Au NPs/MWNT <sup>e</sup> /ITO <sup>f</sup>	0.5–90	0.025		<sup>59</sup>
Au NPs–CNT/GCE	0.03–25	0.01		<sup>60</sup>
TiO <sub>2</sub> <sup>g</sup> /GCE	5–140	0.07		<sup>61</sup>
$\beta$ -CD <sup>h</sup> –MNPs <sup>i</sup> /GCE	0.8–300	0.5		<sup>62</sup>
TS <sup>j</sup> /GCE	1.0–400	0.2		<sup>63</sup>
NiO <sup>k</sup> /CNT/PEDOT <sup>l</sup>	1–41	0.21	0.92	<sup>64</sup>
RGO <sup>m</sup> /SnO <sub>2</sub> /GCE	0.8–300	0.316	0.0451	<sup>65</sup>
Pd <sup>n</sup> –Cu <sup>o</sup> @Cu <sub>2</sub> O <sup>p</sup> /N-RGO	0.01–40	0.0019	0.3923	<sup>66</sup>
AHNSA <sup>q</sup> /RGO/GCE	0.05–200	0.031	0.0451	<sup>67</sup>
SnO <sub>2</sub> –Co <sub>3</sub> O <sub>4</sub> @rGO/IL <sup>r</sup> /CPE <sup>s</sup>	0.02–6	0.0032		<sup>68</sup>
MGO <sup>t</sup> –CD/GCE	0.5–750	0.31		<sup>69</sup>
Nafon-MIP-MWCNTs@IL <sup>u</sup> /GCE	0.008–26	0.006		<sup>70</sup>
C <sub>40</sub> H <sub>38</sub> N <sub>4</sub> CuO <sub>2</sub>	7–48	0.185	3.156	<sup>71</sup>
CSOH/rGO/GCE	0.05–175.8	0.002	0.21 $\mu\text{A } \mu\text{M}^{-1} \text{ cm}^{-2}$	this work

<sup>a</sup>Tetrabutylammonium bromide. <sup>b</sup>Carbon. <sup>c</sup>Copper hexacyanoferrate film modification on cysteamine–gold nanoparticle–graphite–wax. <sup>d</sup>Gold nanoparticles. <sup>e</sup>Multiwalled carbon nanotubes. <sup>f</sup>Indium tin oxide. <sup>g</sup>Titanium dioxide. <sup>h</sup>Betacyclodextrin. <sup>i</sup>Magnetic nanoparticles. <sup>j</sup>Silicon-doped nano-titanium dioxide. <sup>k</sup>Nickel oxide. <sup>l</sup>Poly(3,4-ethylenedioxythiophene). <sup>m</sup>Reduced graphene oxide. <sup>n</sup>Palladium. <sup>o</sup>Copper. <sup>p</sup>Copper oxide. <sup>q</sup>4-Amino-3-hydroxy-1-naphthalene sulfonic acid. <sup>r</sup>Ionic liquid. <sup>s</sup>Carbon past electrode. <sup>t</sup>Magnetic graphene oxide. <sup>u</sup>Molecularly imprinted copolymer–ionic liquid-functionalized multiwalled carbon nanotubes.

Therefore, the oxidation process of L-Trp involves the two-electron transfer, which agrees with reported literature. The  $E^0$  value at CSOH/rGO-modified GCE can be assumed as the plot of  $E_{pa}$  versus scan rate on the ordinate by extrapolating to  $v = 0$  (figure not shown). The value of  $k^0$  can be  $1.514 \times 10^3 \text{ s}^{-1}$ .

**Detection Performance for L-Trp at CSOH/rGO/GCE.** The CSOH/rGO-modified GCE was used to determine L-Trp with

the DPV technique. The corresponding peak current of L-Trp increased proportionally with increasing concentration of L-Trp (Figure 8a). The pot of oxidation peak current versus concentration exhibited good linearity in the range of 0.05–175.8  $\mu\text{M}$ , characterized by the linear regression equation  $I_{pa}$  ( $\mu\text{A}$ ) =  $14.5 C [\mu\text{M}] + 0.4748$  ( $R^2 = 0.9955$ ) (see Figure 8b). In addition, the obtained detection limit is 0.002  $\mu\text{M}$  based on the

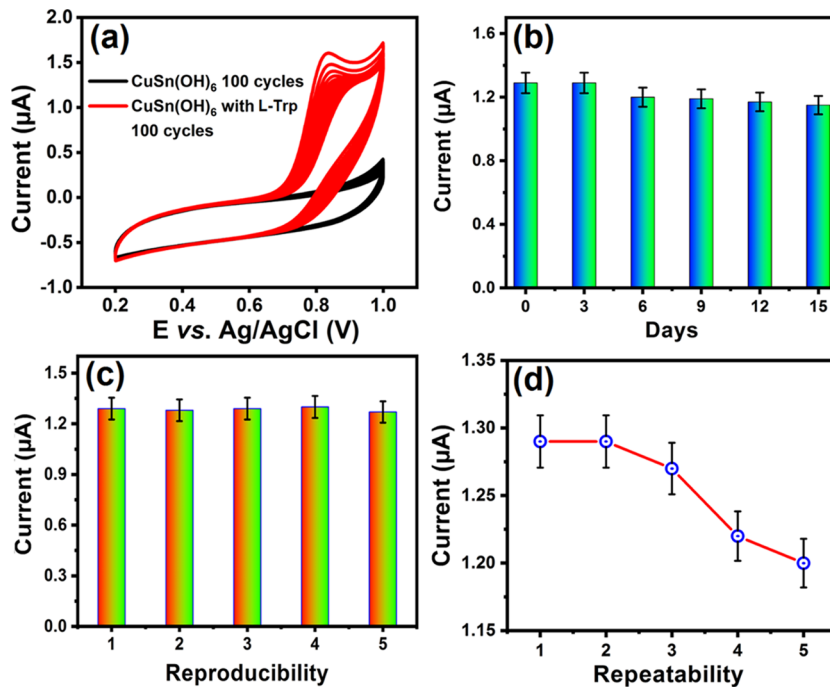


**Figure 9.** (a) Cyclic stability of CSOH/rGO with and without the addition of 50  $\mu\text{M}$  L-Trp (100 cycles), (b) long-term stability, (c) reproducibility, and (d) repeatability. All experiments were conducted in  $\text{N}_2$ -saturated 0.05 M PB (pH 7.0) with a scan rate at 50  $\text{mV s}^{-1}$ .

S/N ratio of 3 (where  $N$  and  $S$  represent the slope of calibration plot and standard deviation of blank response, respectively). To further highlight the sensing advantage of the fabricated sensor, a comparison of the analytical parameters obtained for the L-Trp sensing in the study with previous reports is listed in Table 1. It is also remarkable that the simple process, high stability, and lower LOD of L-Trp observed over CSOH/rGO/GCE is superior to other modified electrodes. For instance, TBAB $\cdots$  $\beta$ -CD/MWCNTs/GCE,<sup>28</sup> Ag@C/GCE,<sup>54</sup> Cys-AuNp-GW,<sup>55</sup> AuNPs/GCE,<sup>58</sup> AuNPs/MWNT/ITO,<sup>59</sup> AuNPs-CNT/GCE,<sup>60</sup> TiO<sub>2</sub>/GCE,<sup>61</sup>  $\beta$ -CD-MNPs/GCE,<sup>62</sup> TS/GCE,<sup>63</sup> NiO/CNT/PEDOT,<sup>64</sup> RGO/SnO<sub>2</sub>,<sup>65</sup> Pd-Cu@Cu<sub>2</sub>O/N-RGO,<sup>66</sup> AHNSA/RGO/GCE,<sup>67</sup> SnO<sub>2</sub>-Co<sub>3</sub>O<sub>4</sub>@rGO/IL,<sup>68</sup> MGO-CD/GCE,<sup>69</sup> Nafon-MIP-MWCNTs@IL,<sup>70</sup> and C<sub>40</sub>H<sub>38</sub>N<sub>4</sub>CuO<sub>2</sub><sup>71</sup> are summarized in Table 1.<sup>28,54,58-71</sup> Despite the fact that noble-metal-doped composites (Ag@C/GCE,<sup>54</sup> AuNPs/GCE,<sup>58</sup> AuNPs/MWNT/ITO,<sup>59</sup> AuNPs-CNT/GCE,<sup>60</sup> and Pd-Cu@Cu<sub>2</sub>O/N-RGO<sup>66</sup>) exhibited excellent catalytic activity toward electrochemical sensing of L-Trp, this process is complex and expensive, compared with the CSOH/rGO-modified electrode. In addition, Cu is recognized as a potentially effective material that is able to enhance the specific capacity of an electrode, and is frequently taken into account mainly because of economic consideration and its large abundance. It is actually less expensive, compared with Ag,<sup>54</sup> Au,<sup>58-60</sup> and Pd.<sup>67</sup> The molecularly imprinted polymer (MIP) is highly selective and affinitive for the analytes but suffers from long extraction time, possibility to degrade temperature-sensitive polymers, large quantity of organic solvent usage, etc. It is difficult to automate the technique or promote solvent flow through MIP.<sup>70</sup> Further, the major disadvantage associated with the copper(II) complex (i.e., C<sub>40</sub>H<sub>38</sub>N<sub>4</sub>CuO<sub>2</sub>) is its instability in the presence of strong reductants.<sup>71</sup> CuSn(OH)<sub>6</sub> exhibits unique optical, electronic, and catalytic properties that have drawn considerable attention in the scientific research community as well as in prospective industrial applica-

tions.<sup>4-15,43,45</sup> In the present work, we have synthesized CuSn(OH)<sub>6</sub> via the co-precipitation method, which has been used for L-Trp sensing. These results prove that CSOH/rGO/GCE is an advantageous platform for the sensing of L-Trp. The current density versus different concentrations of L-Trp was described by the characteristic oxidation peaks (see Figure S6), and the fabricated sensor was displayed to have a high sensitivity of 0.21  $\mu\text{A } \mu\text{M}^{-1} \text{ cm}^{-2}$ . Notably, this fabricated sensor is advantageous for its WLR, high sensitivity, and very low LOD for the electrochemical determination of L-Trp compared to other published sensors (see Table 1).

**Simultaneous Detection.** To find the effect of interference, the CV response of the oxidation peak current of 45  $\mu\text{M}$  L-Trp in the presence of an increasing concentration of uric acid (0–1033  $\mu\text{M}$ ) is shown in Figure 8c. It can be seen clearly that the oxidation peak of uric acid at 0.42 V was well separated from the L-Trp peak at 0.76 V. No substantial deviation in the peak potential and peak current of L-Trp (signal changes only less than 13.3%) was observed. On the other hand, other potential interference of 500  $\mu\text{M}$  organic compounds (such as dopamine, ascorbic acid, D-glucose, L-alanine, and L-threonine) and 500  $\mu\text{M}$  common metal and nonmetal ions (such as Na<sup>+</sup>, K<sup>+</sup>, Mg<sup>2+</sup>, Zn<sup>2+</sup>, Cl<sup>-</sup>, NO<sub>3</sub><sup>-</sup>, and SO<sub>4</sub><sup>2-</sup>) is shown in Figure 8d. It was found that there is no significant interference (signal changes <5%). It was concluded that the fabricated sensor confers a selective method for the detection of L-Trp in the presence of various interfering compounds.

**Stability, Reproducibility, and Repeatability.** The stability was measured by 100 cycles, with 50  $\mu\text{M}$  L-Trp in 0.05 M PB (pH 7.0). Figure 9a shows the 100 CV cycles of the absence and presence of L-Trp. In the absence of L-Trp, no redox peak appeared, showing excellent stability. In addition, in the presence of L-Trp, only less than 10% oxidation peak current decreased, confirming excellent stability. Moreover, the storage stability was studied by determining 20  $\mu\text{M}$  L-Trp in 0.05 M PB (pH 7.0) using the modified electrode stored at 4 °C for 15 days.

Less than 5 % decreased after 15 days of storage. Excellent stability of the fabricated sensor has been achieved (see Figure 9b).

The reproducibility of the fabricated electrode was calculated through DPV curves of five different modified electrodes prepared under the optimal conditions in 0.05 M PB (pH 7.0) containing 10  $\mu\text{M}$  L-Trp. The obtained RSD value was from 1.84 to 3.61%. The results display that the proposed sensor has good reproducibility, as shown in Figure 9c. The repeatability of CSOH/rGO/GCE was calculated through DPV response of six times measurements using the same electrode in 0.05 M PB (pH 7.0) containing 10  $\mu\text{M}$  L-Trp. Experimental results show that the RSD value from 1.67 to 2.89%, suggesting that the fabricated electrode keeps good repeatability (see Figure 9d).

**Real Samples Tests.** To execute the reliability of the fabricated L-Trp sensor, the CSOH/rGO composite-based electrochemical sensor was used to determine L-Trp in different human urine (HU) samples (Figure S7). The real samples were collected from healthy volunteer patients. Then, human urine samples were diluted 10-fold in 0.05 M PB (pH 7.0). Table 2

**Table 2. Determination of L-Trp in Human Urine Samples by DPV ( $n = 3$ )**

human urine (HU, $\mu\text{M}$ )	concentration			
	added ( $\mu\text{M}$ )	found ( $\mu\text{M}$ )	recovery (%)	RSD (%)
HU sample 1	0.6	0.56	93.4	4.81
	1.6	1.54	96.3	4.74
	2.2	2.16	98.3	3.80
	3.4	3.34	98.2	3.84
	5.4	5.38	99.6	3.32
	7.4	7.36	99.4	2.30
	9.2	9.17	99.6	2.14
	12.0	11.92	99.3	2.37
	14.2	14.17	99.7	2.16
	17	16.73	98.4	2.63
	21.8	21.80	99.4	1.84
	0.6	0.57	95.0	3.62
	1.6	1.52	95.0	3.83
HU sample 2	2.2	2.18	99.0	3.70
	3.4	3.36	98.8	3.80
	5.4	5.33	98.7	2.96
	7.4	7.35	99.3	2.37
	9.2	9.11	99.0	2.34
	12	11.92	99.3	2.39
	14.2	14.10	99.2	2.36
	16.8	16.63	98.9	2.63
	21.8	21.64	99.2	1.74

lists the observed data of the DPV current value. The satisfactory recoveries were 93.4–99.7% with RSD values of 1.84–4.81%. The results indicate that the CSOH/rGO composite-based sensor can accurately determine L-Trp in the real samples test and is suitable for practical applications.

## CONCLUSIONS

We report here a simple and cost-efficient co-precipitation strategy for preparing CSOH/rGO composite. The SEM, TEM, XRD, FT-IR, and XPS characterizations clearly showed the formation of highly porous CSOH/rGO composite. In terms of the CSOH/rGO/GCE composite-modified electrode, the electrochemical sensing properties for the detection of L-Trp

were studied by different electrochemical techniques. The electrochemical measurements showed that CSOH/rGO/GCE has excellent sensing performance for L-Trp detection. Compared with the previously reported electrode materials, the present CSOH/rGO-modified electrode system exhibited larger and more sensitive current response and lower LOD (0.002  $\mu\text{M}$ ) and WLR (0.05–175.8  $\mu\text{M}$ ) toward L-Trp. Moreover, the CSOH/rGO composite exhibited excellent sensing selectivity, sensitivity (0.21  $\mu\text{A} \mu\text{M}^{-1} \text{cm}^{-2}$ ), and reproducibility for L-Trp detection in the presence of high concentration of organic compounds (such as dopamine, ascorbic acid, D-glucose, L-alanine, and L-threonine) and common metal and nonmetal ions (such as  $\text{Na}^+$ ,  $\text{K}^+$ ,  $\text{Mg}^{2+}$ ,  $\text{Na}^{2+}$ ,  $\text{Zn}^{2+}$ ,  $\text{Cl}^-$ ,  $\text{NO}_3^-$ , and  $\text{SO}_4^{2-}$ ) interferents. In addition, the CSOH/rGO composite has also been successfully used for the detection of L-Trp in different real human urine samples.

## ASSOCIATED CONTENT

### Supporting Information

The Supporting Information is available free of charge at <https://pubs.acs.org/doi/10.1021/acs.jpcc.0c07197>.

Characterization techniques; experimental results from SEM, EDX, and DPV studies ([PDF](#))

## AUTHOR INFORMATION

### Corresponding Authors

**Shen-Ming Chen** – Department of Chemical Engineering and Biotechnology, National Taipei University of Technology, Taipei 10608, Taiwan, ROC; Department of Chemistry, National Taiwan University, Taipei 10617, Taiwan, ROC;  [orcid.org/0000-0002-0132-9161](https://orcid.org/0000-0002-0132-9161); Phone: +886-2-27017147; Email: [smchen78@ms15.hinet.net](mailto:smchen78@ms15.hinet.net); Fax: +886-2-27025238

**Pitchaimani Veerakumar** – Department of Chemistry, National Taiwan University, Taipei 10617, Taiwan, ROC; Institute of Atomic and Molecular Sciences, Academia Sinica, Taipei 10617, Taiwan, ROC;  [orcid.org/0000-0002-6899-9856](https://orcid.org/0000-0002-6899-9856); Phone: +886-2-23668230; Email: [spveerakumar@gmail.com](mailto:spveerakumar@gmail.com); Fax: +886-2-23620200

**King-Chuen Lin** – Department of Chemistry, National Taiwan University, Taipei 10617, Taiwan, ROC; Institute of Atomic and Molecular Sciences, Academia Sinica, Taipei 10617, Taiwan, ROC;  [orcid.org/0000-0002-4933-7566](https://orcid.org/0000-0002-4933-7566); Phone: +886-2-33661162; Email: [kcln@ntu.edu.tw](mailto:kcln@ntu.edu.tw)

### Authors

**Arumugam Sangili** – Department of Chemical Engineering and Biotechnology, National Taipei University of Technology, Taipei 10608, Taiwan, ROC

**Venkatachalam Vinothkumar** – Department of Chemical Engineering and Biotechnology, National Taipei University of Technology, Taipei 10608, Taiwan, ROC

**Chia-Wei Chang** – Department of Chemical Engineering and Biotechnology, National Taipei University of Technology, Taipei 10608, Taiwan, ROC

**I. Panneer Muthuselvam** – Department of Physics (MMV), Banaras Hindu University, 221005 Uttar Pradesh, India

Complete contact information is available at:

<https://pubs.acs.org/10.1021/acs.jpcc.0c07197>

### Author Contributions

<sup>†</sup>A.S. and V.V. contributed equally to this work.

**Notes**

The authors declare no competing financial interest.

**ACKNOWLEDGMENTS**

The authors are grateful for the financial support (MOST 106-2113-M-027-003-MY3 to SMC; MOST-102-2113-M-002-009-MY3 to KCL) from the Ministry of Science and Technology (MOST), Taiwan. I.P.M. acknowledges the Department of Science and Technology in India for support of INSPIRE Faculty Award DST/INSPIRE/04/2016/002275 (No. IFA16-PH171).

**REFERENCES**

- (1) Jiang, Y.-F.; Jiang, N.; Liang, K.; Yuan, C.-Z.; Fang, X.-X.; Xu, A.-W. A simple and general route to prepare functional mesoporous double-metal oxy(hydroxide). *J. Mater. Chem. A* **2019**, *7*, 7932–7938.
- (2) Najorka, J.; Kleppe, A. K.; Welch, M. D. The effect of pressure and composition on Cu-bearing hydroxide perovskite. *Phys. Chem. Miner.* **2019**, *46*, 877–887.
- (3) Jia, X. H.; Tian, M. G.; Zhang, Z.; Dai, R. R.; Wu, X. Y.; Song, H. J. Highly sensitive formaldehyde chemical sensor based on in situ precipitation synthesis of  $ZnSnO_3$  microspheres. *J. Mater. Sci.: Mater. Electron.* **2015**, *26*, 6224–6231.
- (4) Xu, X. X.; Duan, G. T.; Li, Y.; Zhang, H. W.; Liu, G. Q.; Cai, W. P. Synthesis of nano-cubic  $ZnSn(OH)_3$  based on stannate reaction with liquid laser ablation-induced  $ZnO$  below room temperature. *CrystEngComm* **2013**, *15*, 6159–6164.
- (5) Zhong, S. L.; Xu, R.; Wang, L.; Li, Y.; Zhang, L. F.  $CuSn(OH)_6$  submicrospheres: room temperature synthesis, growth mechanism, and weak antiferromagnetic behavior. *Mater. Res. Bull.* **2011**, *46*, 2385–2391.
- (6) Lin, X.; Gao, Y.; Jiang, M.; Zhang, Y.; Hou, Y.; Dai, W.; Wang, S.; Ding, Z. Photocatalytic  $CO_2$  reduction promoted by uniform perovskite hydroxide  $CoSn(OH)_6$  nanocubes. *Appl. Catal., B* **2018**, *224*, 1009–1016.
- (7) Liu, H.; Ding, Y.-N.; Bian, B.; Li, L.; Li, R.; Zhang, X.; Liu, Z.; Zhang, X.; Fan, G.; Liu, Q. Rapid colorimetric determination of dopamine based on the inhibition of the peroxidase mimicking activity of platinum loaded  $CoSn(OH)_6$  nanocubes. *Microchim. Acta* **2019**, *186*, No. 755.
- (8) Kramer, J. W.; Isaacs, S. A.; Manivannan, V. Microwave-assisted metathesis synthesis of schoenfliesite-type  $MSn(OH)_6$  ( $M = Mg, Ca, Zn$ , and  $Sr$ ) materials. *J. Mater. Sci.* **2009**, *44*, 3387–3392.
- (9) Cheng, P.; Ni, Y.; Yuan, K.; Hong, J. Fast sonochemical synthesis of  $CoSn(OH)_6$  nanocubes, conversion towards shape-preserved  $SnO_2$ – $Co_3O_4$  hybrids and their photodegradation properties. *Mater. Lett.* **2013**, *90*, 19–22.
- (10) Jena, H.; Kutty, K. G.; Kutty, T. R. N. Ionic transport and structural investigations on  $MSn(OH)_6$  ( $M = Ba, Ca, Mg, Co, Zn, Fe, Mn$ ) hydroxide perovskites synthesized by wet sonochemical methods. *Mater. Chem. Phys.* **2004**, *88*, 167–179.
- (11) Dong, S.; Cui, L.; Zhao, Y.; Wu, Y.; Xia, L.; Su, X.; Zhang, C.; Wang, D.; Guo, W.; Sun, J. Crystal structure and photocatalytic properties of perovskite  $MSn(OH)_6$  ( $M = Cu$  and  $Zn$ ) composites with  $d^{10}$ – $d^{10}$  configuration. *Appl. Surf. Sci.* **2019**, *463*, 659–667.
- (12) Sahoo, R.; Sasmal, A. K.; Ray, C.; Dutta, S.; Pal, A.; Pal, T. Suitable morphology makes  $CoSn(OH)_6$  nanostructure a superior electrochemical pseudocapacitor. *ACS Appl. Mater. Interfaces* **2016**, *8*, 17987–17998.
- (13) Zhang, Y.; Zhou, L.; Xiong, F.; Tang, H.; An, Q.; Mai, L. Amorphous  $CuSnO_3$  nanospheres anchored on interconnected carbon networks for use as novel anode materials for high-performance sodium ion batteries. *Inorg. Chem. Front.* **2018**, *5*, 2756–2762.
- (14) Huang, D.; Fu, X.; Long, J.; Jiang, X.; Chang, L.; Meng, S.; Chen, S. Hydrothermal synthesis of  $MSn(OH)_6$  ( $M = Co, Cu, Fe, Mg, Mn, Zn$ ) and their photocatalytic activity for the destruction of gaseous benzene. *Chem. Eng. J.* **2015**, *269*, 168–179.
- (15) Zhou, Z.; Chen, T.; Deng, J.; Yao, Q.; Wang, Z.; Zhou, H.  $CuSn(OH)_6$  nanocubes as high-performance anode materials for lithium-ion batteries. *Int. J. Electrochem. Sci.* **2018**, *13*, 2001–2009.
- (16) Li, Y.; Tian, X.; Wang, Y.; Yang, Q.; Diao, Y.; Zhang, B.; Yang, D. In Situ construction of a  $MgSn(OH)_6$  perovskite/ $SnO_2$  type-II heterojunction: A highly efficient photocatalyst towards photodegradation of tetracycline. *Nanomaterials* **2020**, *10*, 53.
- (17) Subbarayan, S.; Natesan, M.; Chen, S.-M. Simple synthesis of  $CoSn(OH)_6$  nanocubes for the rapid electrochemical determination of rutin in the presence of quercetin and acetaminophen. *New J. Chem.* **2020**, *44*, 11271–11281.
- (18) Lee, C.-S.; Shim, S. J.; Kim, T. H. Scalable preparation of low-defect graphene by urea-assisted liquid-phase shear exfoliation of graphite and its application in doxorubicin analysis. *Nanomaterials* **2020**, *10*, 267.
- (19) Saleh, T. A.; Fadillah, G. Recent trends in the design of chemical sensors based on graphene-metal oxide nanocomposites for the analysis of toxic species and biomolecules. *TrAC, Trends Anal. Chem.* **2019**, *120*, No. 115660.
- (20) Sahu, S.; Sahoo, M. R.; Kushwaha, A. K.; Rout, G. C.; Nayak, S. K. Charge transfer and hybridization effect at the graphene-nickel interface: A tight binding model study. *Carbon* **2019**, *142*, 685–696.
- (21) Rowley-Neale, S. J.; Randviir, E. P.; Abo Dena, A. S.; Banks, C. E. An overview of recent applications of reduced graphene oxide as a basis of electroanalytical sensing platforms. *Appl. Mater. Today* **2018**, *10*, 218–226.
- (22) Li, X.; Zhao, Y.; Wang, X.; Wang, J.; Gaskov, A. M.; Akbar, S. A. Reduced graphene oxide (rGO) decorated  $TiO_2$  microspheres for selective room-temperature gas sensors. *Sens. Actuators, B Chem.* **2016**, *230*, 330–336.
- (23) Qureshi, K.; Ahmad, M. Z.; Bhatti, I. A.; Zahid, M.; Nisar, J.; Iqbal, M. Graphene oxide decorated  $ZnWO_4$  architecture synthesis, characterization and photocatalytic activity evaluation. *J. Mol. Liq.* **2019**, *285*, 778–789.
- (24) Wang, Q.; Wu, X.; Zhang, L. Designed of bifunctional Z-scheme  $CuSnO_3@Cu_2O$  heterojunctions film for photoelectrochemical catalytic reduction and ultrasensitive sensing nitrobenzene. *Chem. Eng. J.* **2019**, *361*, 398–407.
- (25) Yang, J.; Ye, H.; Zhang, Z.; Zhao, F.; Zeng, B. Metal–organic framework derived hollow polyhedron  $CuCo_2O_4$  functionalized porous graphene for sensitive glucose sensing. *Sens. Actuators. B-Chem.* **2017**, *242*, 728–735.
- (26) He, Q.; Tian, Y.; Wu, Y.; Liu, J.; Li, G.; Deng, P.; Chen, D. Electrochemical sensor for rapid and sensitive detection of tryptophan by a  $Cu_2O$  nanoparticles-coated reduced graphene oxide nanocomposite. *Biomolecules* **2019**, *9*, 176.
- (27) He, Q.; Liu, J.; Feng, J.; Wu, Y.; Tian, Y.; Li, G.; Chen, D. Sensitive voltammetric sensor for tryptophan detection by using polyvinylpyrrolidone functionalized graphene/GCE. *Nanomaterials* **2020**, *10*, 125.
- (28) Mukdasai, S.; Poosittisak, S.; Ngeontae, W.; Srijaranai, S. A highly sensitive electrochemical determination of L-tryptophan in the presence of ascorbic acid and uric acid using in situ addition of tetrabutylammonium bromide on the  $\beta$ -cyclodextrin incorporated multi-walled carbon nanotubes modified electrode. *Sens. Actuators, B Chem.* **2018**, *272*, 518–525.
- (29) Zhou, S.; Deng, Z.; Wu, Z.; Xie, M.; Tian, Y.; Wu, Y.; Liu, J.; Li, G.; He, Q.  $Ta_2O_5/rGO$  nanocomposite-modified electrodes for detection of tryptophan through electrochemical route. *Nanomaterials* **2019**, *9*, 811.
- (30) Kochen, W.; Steinhart, H. *L-Tryptophan: Current Prospects in Medicine and Drug Safety*; Walter de Gruyter: Berlin, Germany, 1994.
- (31) Zhen, Q.; Xu, B.; Ma, L.; Tian, G.; Tang, X.; Ding, M. Simultaneous determination of tryptophan, kynurenone and 5-hydroxytryptamine by HPLC: Application in uremic patients undergoing hemodialysis. *Clin. Biochem.* **2011**, *44*, 226–230.
- (32) Ren, J.; Zhao, M.; Wang, J.; Cui, C.; Yang, B. Spectrophotometric method for determination of tryptophan in protein hydrolysates. *Food Technol. Biotechnol.* **2007**, *45*, 360–366.

- (33) Ilisz, I.; Fodor, G.; Berkecz, R.; Iványi, R.; Szente, L.; Péter, A. Enantioseparation of  $\beta$ -substituted tryptophan analogues with modified cyclodextrins by capillary zone electrophoresis. *J. Chromatogr. A* **2009**, *1216*, 3360–3365.
- (34) Miller, G. D.; Johnson, J. A.; Miller, B. S. Fluorometric micromethod for determination of tryptophan. *Anal. Chem.* **1956**, *28*, 884–887.
- (35) Liang, Y. D.; Song, J. F. Flow-injection chemiluminescence determination of tryptophan through its peroxidation and epoxidation by peroxy nitrous acid. *J. Pharm. Biomed. Anal.* **2005**, *38*, 100–106.
- (36) Tang, X.; Liu, Y.; Hou, H.; You, T. Electrochemical determination of L-tryptophan, L-tyrosine and L-cysteine using electrospun carbon nanofibers modified electrode. *Talanta* **2010**, *80*, 2182–2186.
- (37) Xia, Y.; Zhao, F.; Zeng, B. A molecularly imprinted copolymer based electrochemical sensor for the highly sensitive detection of L-Tryptophan. *New J. Chem.* **2018**, *42*, 3509–3518.
- (38) Mattioli, I. A.; Baccarin, M.; Cervini, P.; Cavalheiro, É. T. G. Electrochemical investigation of a graphite polyurethane composite electrode modified with electrodeposited gold nanoparticles in the voltammetric determination of tryptophan. *J. Electroanal. Chem.* **2019**, *835*, 212–219.
- (39) Deng, P.; Xu, Z.; Feng, Y. Acetylene black paste electrode modified with graphene as the voltammetric sensor for selective determination of tryptophan in the presence of high concentrations of tyrosine. *Mater. Sci. Eng.: C* **2014**, *35*, 54–60.
- (40) Tian, Y.; Deng, P.; Wu, Y.; Ding, Z.; Li, G.; Liu, J.; He, Q. A simple and efficient molecularly imprinted electrochemical sensor for the selective determination of tryptophan. *Biomolecules* **2019**, *9*, 294.
- (41) Xia, X.; Zheng, Z.; Zhang, Y.; Zhao, X.; Wang, C. Synthesis of Ag-MoS<sub>2</sub>/chitosan nanocomposite and its application for catalytic oxidation of tryptophan. *Sens. Actuators, B Chem.* **2014**, *192*, 42–50.
- (42) Miao, Y.; Ma, Y.; Wang, Q. Plasma-assisted simultaneous reduction and nitrogen/sulfur co-doping of graphene oxide for high-performance supercapacitors. *ACS Sustain. Chem. Eng.* **2019**, *7*, 7597–7608.
- (43) Liu, H.; Ding, Y. N.; Yang, B.; Liu, Z.; Zhang, X.; Liu, Q. Iron doped CuSn(OH)<sub>6</sub> microspheres as a peroxidase-mimicking artificial enzyme for H<sub>2</sub>O<sub>2</sub> colorimetric detection. *ACS Sustain. Chem. Eng.* **2018**, *11*, 14383–14393.
- (44) Wang, L.; Tang, K.; Liu, Z.; Wang, D.; Sheng, J.; Cheng, W. Single-crystalline ZnSn(OH)<sub>6</sub> hollow cubes via self-templated synthesis at room temperature and their photocatalytic properties. *J. Mater. Chem.* **2011**, *21*, 4352–4357.
- (45) Sangili, A.; Annalakshmi, M.; Chen, S. M.; Balasubramanian, P.; Sundarajan, M. Synthesis of silver nanoparticles decorated on core-shell structured tannic acid-coated iron oxide nanospheres for excellent electrochemical detection and efficient catalytic reduction of hazardous 4-nitrophenol. *Composites, Part B* **2019**, *162*, 32–42.
- (46) Ahmad, K.; Mohammad, A.; Ansari, S. N.; Mobin, S. M. Construction of graphene oxide sheets based modified glassy carbon electrode (GO/GCE) for the highly sensitive detection of nitrobenzene. *Mater. Res. Express* **2018**, *5*, No. 075601.
- (47) Huang, H.; Yue, Y.; Chen, Z.; Chen, Y.; Wu, S.; Liao, J.; Liu, S.; Wen, H. Electrochemical sensor based on a nanocomposite prepared from TmPO<sub>4</sub> and graphene oxide for simultaneous voltammetric detection of ascorbic acid, dopamine and uric acid. *Microchim. Acta* **2019**, *186*, 189.
- (48) Zhu, S.; Zhang, J.; Zhao, X.; Wang, H.; Xu, G.; You, J. Electrochemical behavior and voltammetric determination of L-tryptophan and L-tyrosine using a glassy carbon electrode modified with single-walled carbon nanohorns. *Microchim. Acta* **2014**, *181*, 445–451.
- (49) Wang, G.; Wei, Y.; Zhang, W.; Zhang, X.; Fang, B.; Wang, L. Enzyme-free amperometric sensing of glucose using Cu-CuO nanowire composites. *Microchim. Acta* **2010**, *168*, 87–92.
- (50) Akpotu, S. O.; Moodley, B. Encapsulation of silica nanotubes from elephant grass with graphene oxide/reduced graphene oxide and its application in remediation of sulfamethoxazole from aqueous media. *ACS Sustain. Chem. Eng.* **2018**, *6*, 4539–4548.
- (51) Jin, G. P.; Lin, X. Q. The electrochemical behavior and amperometric determination of tyrosine and tryptophan at a glassy carbon electrode modified with butyrylcholine. *Electrochim. Commun.* **2004**, *6*, 454–460.
- (52) Yu, X.; Mai, Z.; Xiao, Y.; Zou, X. Electrochemical behavior and determination of L-tyrosine at single-walled carbon nanotubes modified glassy carbon electrode. *Electroanalysis* **2008**, *20*, 1246–1251.
- (53) Özcan, A.; Şahin, Y. A novel approach for the selective determination of tryptophan in blood serum in the presence of tyrosine based on the electrochemical reduction of oxidation product of tryptophan formed in situ on graphite electrode. *Biosens. Bioelectron.* **2012**, *31*, 26–31.
- (54) Mao, S.; Li, W.; Long, Y.; Tu, Y.; Deng, A. Sensitive electrochemical sensor of tryptophan based on Ag@C core–shell nanocomposite modified glassy carbon electrode. *Anal. Chim. Acta* **2012**, *738*, 35–40.
- (55) Prabhu, P.; Babu, R. S.; Narayanan, S. S. Electrocatalytic oxidation of L-tryptophan using copper hexacyanoferate film modified gold nanoparticle graphite-wax electrode. *Colloids Surf., B* **2011**, *87*, 103–108.
- (56) Wang, Y.; Ouyang, X.; Ding, Y.; Liu, B.; Xu, D.; Liao, L. An electrochemical sensor for determination of tryptophan in the presence of DA based on poly(L-methionine)/graphene modified electrode. *RSC Adv.* **2016**, *6*, 10662–10669.
- (57) Zhao, P.; Ni, M.; Xu, Y.; Wang, C.; Chen, C.; Zhang, X.; Li, C.; Xie, Y.; Fei, J. A novel ultrasensitive electrochemical quercetin sensor based on MoS<sub>2</sub>-carbon nanotube@graphene oxide nanoribbons/HS-cyclodextrin/graphene quantum dots composite film. *Sens. Actuators, B Chem.* **2019**, *299*, 126997–127008.
- (58) Li, C.; Ya, Y.; Zhan, G. Electrochemical investigation of tryptophan at gold nanoparticles modified electrode in the presence of sodium dodecylbenzene sulfonate. *Colloids Surf., B* **2010**, *76*, 340–345.
- (59) Goyal, R. N.; Bishnoi, S.; Chasta, H.; Aziz, M. A.; Oyama, M. Effect of surface modification of indium tin oxide by nanoparticles on the electrochemical determination of tryptophan. *Talanta* **2011**, *85*, 2626–2631.
- (60) Guo, Y.; Guo, S.; Fang, Y.; Dong, S. Gold nanoparticle/carbon nanotube hybrids as an enhanced material for sensitive amperometric determination of tryptophan. *Electrochim. Acta* **2010**, *55*, 3927–3931.
- (61) Fan, Y.; Liu, J. H.; Lu, H. T.; Zhang, Q. Electrochemistry and voltammetric determination of L-tryptophan and L-tyrosine using a glassy carbon electrode modified with a Nafion/TiO<sub>2</sub>-graphene composite film. *Microchim. Acta* **2011**, *173*, 241–247.
- (62) Wang, H.; Zhou, Y.; Guo, Y.; Liu, W.; Dong, C.; Wu, Y.; Li, S.; Shuang, S.  $\beta$ -cyclodextrin/Fe<sub>3</sub>O<sub>4</sub> hybrid magnetic nano-composite modified glassy carbon electrode for tryptophan sensing. *Sens. Actuators, B Chem.* **2012**, *163*, 171–178.
- (63) Wan, M.; Li; Long, Y.; Tu, Y. Electrochemical determination of tryptophan based on Si-doped nano-TiO<sub>2</sub> modified glassy carbon electrode. *Anal. Methods* **2012**, *4*, 2860–2865.
- (64) Sun, D.; Li, H.; Li, M.; Li, C.; Dai, H.; Sun, D.; Yang, B. Electrodeposition synthesis of a NiO/CNT/PEDOT composite for simultaneous detection of dopamine, serotonin, and tryptophan. *Sens. Actuators, B Chem.* **2018**, *259*, 433–442.
- (65) Haldorai, Y.; Yeon, S. H.; Huh, Y. S.; Han, Y. K. Electrochemical determination of tryptophan using a glassy carbon electrode modified with flower-like structured nanocomposite consisting of reduced graphene oxide and SnO<sub>2</sub>. *Sens. Actuators, B Chem.* **2017**, *239*, 1221–1230.
- (66) Li, J.; Jiang, J.; Xu, Z.; Liu, M.; Tang, S.; Yang, C.; Qian, D. Facile synthesis of Pd–Cu@Cu<sub>2</sub>O/N-RGO hybrid and its application for electrochemical detection of tryptophan. *Microchim. Acta* **2018**, *260*, S26–S35.
- (67) Raj, M.; Goyal, R. N. facile method to anchor reduced graphene oxide polymer nanocomposite on the glassy carbon surface and its application in the voltammetric estimation of tryptophan in presence of S-hydroxytryptamine. *Sens. Actuators. B-Chem.* **2016**, *233*, 445–453.

- (68) Zeinali, H.; Bagheri, H.; Monsef-Khoshhesab, Z.; Khoshhsafar, H.; Hajian, A. Nanomolar simultaneous determination of tryptophan and melatonin by a new ionic liquid carbon paste electrode modified with  $\text{SnO}_2\text{-Co}_3\text{O}_4@\text{rGO}$  nanocomposite. *Mater. Sci. Eng.: C* **2017**, *71*, 386–394.
- (69) Wang, C.; Li, T.; Liu, Z.; Guo, Y.; Li, C.; Dong, C.; Shuang, S. An ultra-sensitive sensor based on  $\beta$ -cyclodextrin modified magnetic graphene oxide for detection of tryptophan. *J. Electroanal. Chem.* **2016**, *781*, 363–370.
- (70) Xia, Y.; Zhao, F.; Zeng, B. A molecularly imprinted copolymer based electrochemical sensor for the highly sensitive detection of *L*-Tryptophan. *Talanta* **2020**, *206*, No. 120245.
- (71) Saini, A. K.; Saraf, M.; Kumari, P.; Mobin, S. M. A highly selective and sensitive chemosensor for *L*-tryptophan by employing a Schiff based Cu(II) complex. *New J. Chem.* **2018**, *42*, 3509–3518.